Research Square

Preprints are preliminary reports that have not undergone peer review.
They should not be considered conclusive, used to inform clinical practice,
or referenced by the media as validated information.

# In-Silico Investigation towards the Non-Invasive Optical Detection of Blood Lactate

**Subhasri Chatterjee** ( subhasri.chatterjee.2@city.ac.uk )
City, University of London
**Karthik Budidha**
City, University of London
**Meha Qassem**
City, University of London
**Panicos A. Kyriacou**
City, University of London

**Research Article**

**Keywords:** Monte Carlo simulations, shortwave infrared (SWIR) light, vascular tissue, blood lactate, optical sensor

**Posted Date:** May 6th, 2021

**DOI:** https://doi.org/10.21203/rs.3.rs-471340/v1

**License:** This work is licensed under a Creative Commons Attribution 4.0 International License.
Read Full License

**Version of Record:** A version of this preprint was published at Scientific Reports on July 12th, 2021. See the published version at https://doi.org/10.1038/s41598-021-92803-x.

# In-Silico Investigation towards the Non-Invasive Optical Detection of Blood Lactate

**Subhasri Chatterjee**[1,*,+], **Karthik Budidha**[1,+], **Meha Qassem**[1], **and Panicos A. Kyriacou**[1]

[1]Research Centre for Biomedical Engineering, City, University of London, London EC1V0HB, UK
[*]Subhasri Chatterjee, subhasri.chatterjee.2@city.ac.uk
[+]these authors contributed equally to this work

## ABSTRACT

This paper uses Monte Carlo simulations to investigate the interaction of short-wave infrared (SWIR) light with vascular tissue as a step toward the development of a non-invasive optical sensor for measuring blood lactate in humans. The primary focus of this work was to determine the optimal source-detector separation, penetration depth of light at SWIR wavelengths in tissue, and the optimal light power required for reliable detection of lactate. The investigation also focused on determining the non-linear variations in absorbance of lactate at a few select SWIR wavelengths. SWIR photons only penetrated 1.3 mm and did not travel beyond the hypodermal fat layer. The maximum output power was only 2.51% of the input power, demonstrating the need for a highly sensitive detection system. Simulations optimized a source-detector separation of 1 mm at 1684 nm for accurate measurement of lactate in blood.

## Introduction

Lactate is a metabolite of glucose produced by the human body during anaerobic energy production. It is transported from the body's tissues to the liver by blood and is either oxidized into carbon dioxide and water or is converted to glucose in a cyclic process. However, this process requires adequate oxygen, and in conditions of hypoperfusion or hypoxia resulting from a severe infection, heart failure or respiratory failure, lactate clearance is hindered, leading to a build-up of lactate in the blood beyond the normal level ($< 2$ mmol/L). This condition, known as lactic acidosis can upset the body's pH balance and often manifests life-threatening symptoms such as difficulty in breathing, confusion, and even coma[1]. Hence a continuous measure of blood lactate is essential in today's critical care for early identification of acute conditions such as sepsis, heart failure, renal failure, severe inflammatory response syndrome, etc.

The prevalence of blood lactate in identifying poor prognosis in acutely ill patients is well known and has been the subject of research for many years. Yet there exists no reliable tool to continuously measure blood lactate reliably and non-invasively in the clinical setting. The state-of-the-art remains to be intermittent measurements using arterial blood gas analyzers, which are invasive, costly, and complex to operate. Hence, there exists an unmet clinical need for a reliable tool that can measure blood lactate non-invasively in the clinical setting.

As a step towards the development of such a device, researchers have investigated the feasibility of using short-wave infrared (SWIR) light (typically, between the range of 1300nm - 2500nm) to detect the optical signature of lactate in blood and estimated the concentration of lactate from the acquired spectra using various regression models[2–8]. These preliminary in-vitro investigations have shown great promise and have paved the way for the development of a novel optical sensor for the blood-lactate measurements. However, these in-vitro experiments are unable to provide any information on the light-tissue interactions underlying the technique, which is key in assessing the efficacy of the sensor design for the lactate measurement. The applicability of a sensor largely depends on the anatomy of the tissue region-of-interest (ROI), and the design of the sensor (e.g., wavelength, shape and size of the optical source and detector, source-detector separations etc.). Such crucial details have so far never been considered. To address these issues, this paper aims to create a robust in-silico model based on preliminary in-vitro experiments, that can be easily modified to simulate any sensor-tissue interaction, thus assisting the development of a novel non-invasive optical sensor for blood lactate detection.

## Background

A number of in-silico and in-vitro models are available in the literature that may help design biophotonic sensors, however, those are mostly limited within the visible and near-infrared optical window. Applications in the short-wave infrared wavelength region remain largely unexplored which can be attributed to the fact that water is highly absorbing at this wavelength range making the analysis difficult to pursue. Recently, a few research works have investigated the SWIR light in vascular tissue with

an interest in optical imaging and diagnosis[9–13]. Unfortunately, none of these models considered the presence of the lactate.

As a part of our previous in-vitro investigation, we found that lactate absorbance peaks are detectable at the SWIR wavelengths even though water absorbance prevails[5]. Figure 1(a) shows the raw spectra (recorded using the Lambda 1050 dual-beam UV/Vis/NIR spectrophotometer, Perkin Elmer Corp, Massachusetts, USA) of sodium L-lactate (L14500, Alfa Aesar, Lancashire, UK) dissolved in aqueous PBS (concentration:100 mmol/L) along with the spectra of an aqueous PBS sample. As can be seen from the figure, water is highly absorbing in the SWIR region, making it difficult to distinguish the lactate absorption from that of water. However, following the subtraction of PBS spectra (water peaks) from the lactate containing spectra as in Figure 1(b), the absorption of lactate and its peaks become evident.

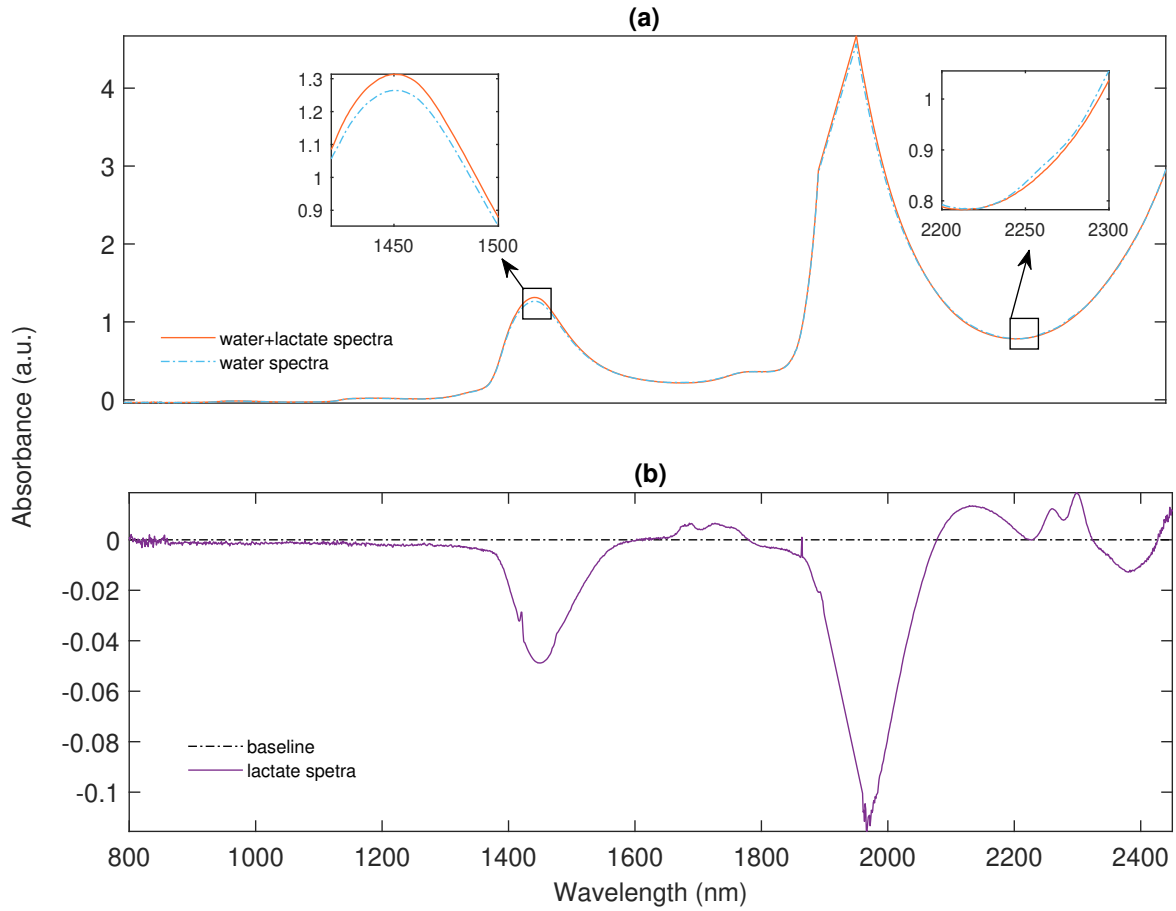


**Figure 1.** (a) The raw spectra of sodium L-lactate dissolved in aqueous PBS (concentration: 100 mmol/L) along with the spectra of just the aqueous PBS solution in the SWIR optical window. (b) Resultant spectra following the subtraction of aqueous PBS spectra from the lactate containing spectra.

Motivated by our initial findings, we have carried out the current in-silico investigation which could aid in the design of an optical sensor for blood-lactate detection. This investigation has been based on the Monte Carlo (MC) modelling method which is one of the most reliable approaches for characterizing a biophotonic sensors[14]. Among several other available tissue-optics models (such as diffusion theory, random walk model, finite element model etc.), Monte Carlo method has been chosen for this study due to its ability to produce accurate results at any source-detector separation, additional to other advantages such as inclusiveness of any complexity of the tissue-structure, multiple random scattering events and any sensor geometry.

## In-silico modelling strategy

A robust MC model of finger-ROI was developed and executed at a reflectance sensor geometry as shown in the schematic diagram in Figure 2. The MC model was explored for determining: (1) the mean penetration depth of light at SWIR wavelengths in vascular tissue, (2) the optimal source-detector separation for the acquisition of lactate spectra and (3) the optimal light power required for reliable detection of lactate concentration in blood.

MC being a strong computational tool has a well-documented limitation regarding its time-consumption. In order to obtain an interpretative outcome within a realistic time frame, we selected *ten* discrete characterizing SWIR wavelengths based on the continuous spectra showed in Figure 1. These wavelengths are 1310 nm, 1550 nm, 1650 nm, 1684 nm, 1730 nm, 1752 nm, 1920 nmm, 2129 nm, 2259 nm and 2299 nm respectively. Simulations were carried out at *three* characterizing source-detector separations that are typically used in the commercial spectrophotometer fibre-optic probes (i.e., 0.7 mm, 1 mm and 1.5 mm).

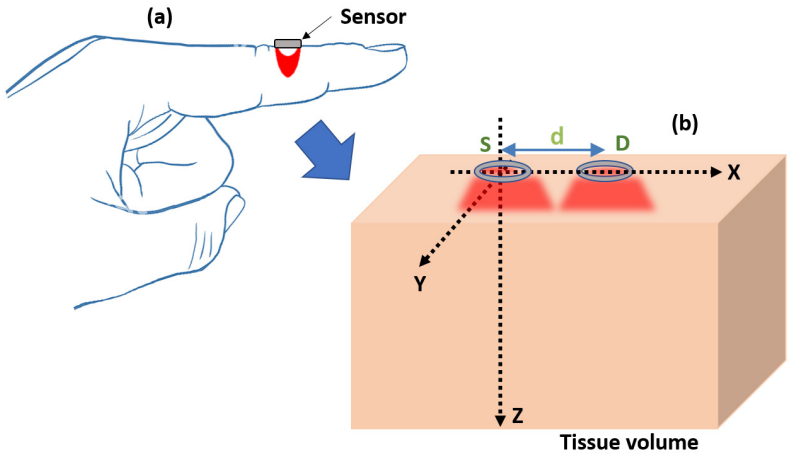


**Figure 2.** Schematic of the sensor-tissue interaction platform. The ROI, i.e., a volume of human finger tissue interrogated by the sensor, is presented in the 3D Cartesian co-ordinate (XYZ) where the optical source (S) and detector (D) are respectively placed at the origin, and a distance $d$ from it.

The anatomical details of a finger-ROI were discussed in our previous publication[15]. A similar model has been used in this work. The semi-infinite tissue-volume had a width and a thickness each of 1.3 cm. The dimension was approximated based on the average measured thickness and width of the index-fingers (phalanx area) of the human volunteers who participated in our previous pilot in-vivo study[15]. The measurement was carried out on eight (5 male and 3 female) healthy human volunteers with age ranging from 20 to 35 years. Necessary ethical approval was gained from the Senate Research Ethics Committee at City, University of London and written informed consent was sought from all the volunteers prior to the commencing of the study. The experiment took place in the Physiological Measurement laboratory of the biomedical engineering research centre at City, University of London. All experiments were performed in accordance with relevant guidelines and regulations.

**Table 1.** Optical properties at SWIR: the absorption coefficients of water ($\mu_{a_w}$), lactate ($\mu_{a_{lact}}$), lipid ($\mu_{a_{lip}}$), melanin ($\mu_{a_{mel}}$); and the scattering coefficients of skin ($\mu_{s_{skin}}$) and hypodermal fat ($\mu_{s_{fat}}$) are illustrated at the characterising wavelengths ($\lambda$).

| $\lambda\,(nm)$ | $\mu_{a_w}\ (mm^{-1})$ | $\mu_{a_{lact}}\ (mm^{-1})$ | $\mu_{a_{lip}}\ (mm^{-1})$ | $\mu_{a_{mel}}\ (mm^{-1})$ | $\mu_{s_{skin}}\ (mm^{-1})$ | $\mu_{a_{fat}}\ (mm^{-1})$ |
|---|---|---|---|---|---|---|
| 1310 | 0.12 | 0.29 | 0.18 | 2.75 | 4.9 | 10.57 |
| 1550 | 1.07 | 0.33 | 0.17 | 1.57 | 3.62 | 9.63 |
| 1650 | 0.48 | 0.35 | 0.15 | 1.27 | 3.25 | 9.47 |
| 1684 | 0.45 | 0.37 | 0.21 | 1.19 | 3.14 | 9.76 |
| 1730 | 0.61 | 0.37 | 0.42 | 1.09 | 3 | 13.74 |
| 1752 | 0.71 | 0.35 | 0.33 | 1.04 | 2.94 | 11.89 |
| 1920 | 11.45 | 0.33 | 0.5 | 0.77 | 2.52 | 14.63 |
| 2129 | 2.2 | 0.43 | 0.29 | 0.54 | 2.13 | 11.79 |
| 2259 | 1.72 | 0.54 | 0.29 | 0.45 | 1.94 | 15.69 |
| 2299 | 2.24 | 0.58 | 0.68 | 0.42 | 1.88 | 22.56 |

In the tissue volume, the stratum corneum and epidermis, the two outermost skin layers, were bloodless, and water made up 5% and 20% of those tissue volumes (including blood plasma), respectively. Dermis was divided into four sublayers depending on the different distributions in blood content at different depths: papillary dermis (0.1mm thick, 4% blood, 50% water), upper blood net dermis (0.08mm thick, 30% blood, 60% water), reticular dermis (0.2mm thick, 4% blood, 70% water), and deep blood net dermis (0.3mm thick, 10% blood, 70% water). Normal and hyperlactatemic physiological conditions were simulated by varying the blood-lactate concentrations through a range of 1-6 mmol/L.

The tissue model was optically characterized at the SWIR wavelengths by - (a) the volumetric distributions of the absorbers (i.e., epidermal melanin, blood lactate, lipid, and water), and (b) the *Rayleigh* and *Mie* scattering distributions by the small and large scale scatterers (i.e., dermal collagen and epidermal keratin). The details of the wavelength-dependent optical parameters (e.g., absorption coefficient $\mu_a$ and scattering coefficient $\mu_s$) are illustrated in Table 1. The lactate and water absorption coefficients were deduced from the optical spectra recorded in our lab and the rest of the parameters were adapted from published literature[14,16–19]. The anisotropy factor ($g = 0.9$) and refractive index ($n = 1.4$) were considered the same at all wavelengths as the variations in such parameters do not influence the model outcomes[17].

The simulated optical source generated Gaussian beam of radius of 0.1mm, and the circular detector was of 0.2mm radius. In each iteration, a large number of photon packets ($10^9 - 10^{10}$) were computed. MATLAB (Mathworks, Inc. USA) platform was chosen for coding and a multi-thread programming environment was used for facilitating the simulation.

## Results

The distribution of the light-tissue interaction events (absorption + scattering) through the dermal and subdermal tissue layers of the finger ROI at different optical sensor geometries are illustrated in Fig. 3. The light-tissue interaction profiles vary

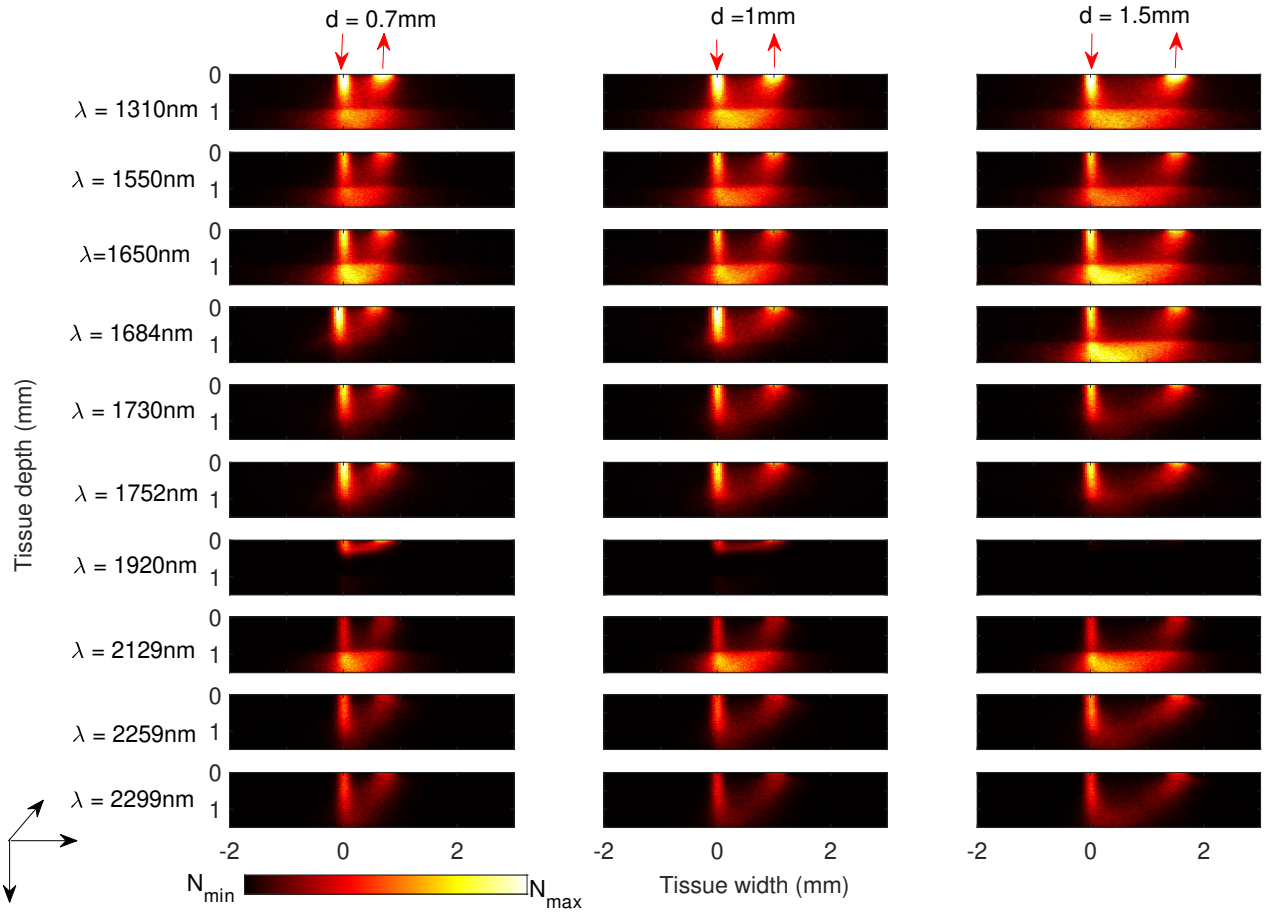


**Figure 3.** Monte Carlo simulated light-tissue interaction profiles. The results show the distribution of the light-tissue interaction events in a reflectance mode optical sensor geometry having a source (downward red arrow) and a detector (upward red arrow). Results at three source-detector separations ($d = 0.7mm,\ 1mm\ and\ 1.5mm$) and the ten SWIR wavelengths ($\lambda$ = 1310 nm, 1550 nm, 1650 nm, 1684 nm, 1730 nm, 1752 nm, 1920 nm, 2129 nm, 2259 nm and 2299 nm) are presented along the columns and the rows, respectively. The colorbar represents the number distribution of the interaction events (N) between its minimum and maximum values.

significantly for different combinations of wavelengths and source-detector separations. Light does not penetrate beyond the hypodermal fat ($\leq 1.5mm$) at any combination of the sensor specifications. At 1920 nm, very few photons are able to penetrate through the tissue-layers because of the very high absorbance at this wavelength. At all simulated wavelengths, light penetrates

through the outermost bloodless skin tissue layers, i.e., stratum corneum and epidermis, and reach the vascularized dermis. The scattering coefficient of the skin collagen reduces exponentially with increasing SWIR wavelength, resulting in lower probability of multiple scattering in the medium[20], hence, fewer light-tissue interaction events through the skin. Scattering in the hypodermis is governed by the lipid droplets[21] which exhibit higher scattering compared to dermis, resulting in multiple light-tissue interaction events.

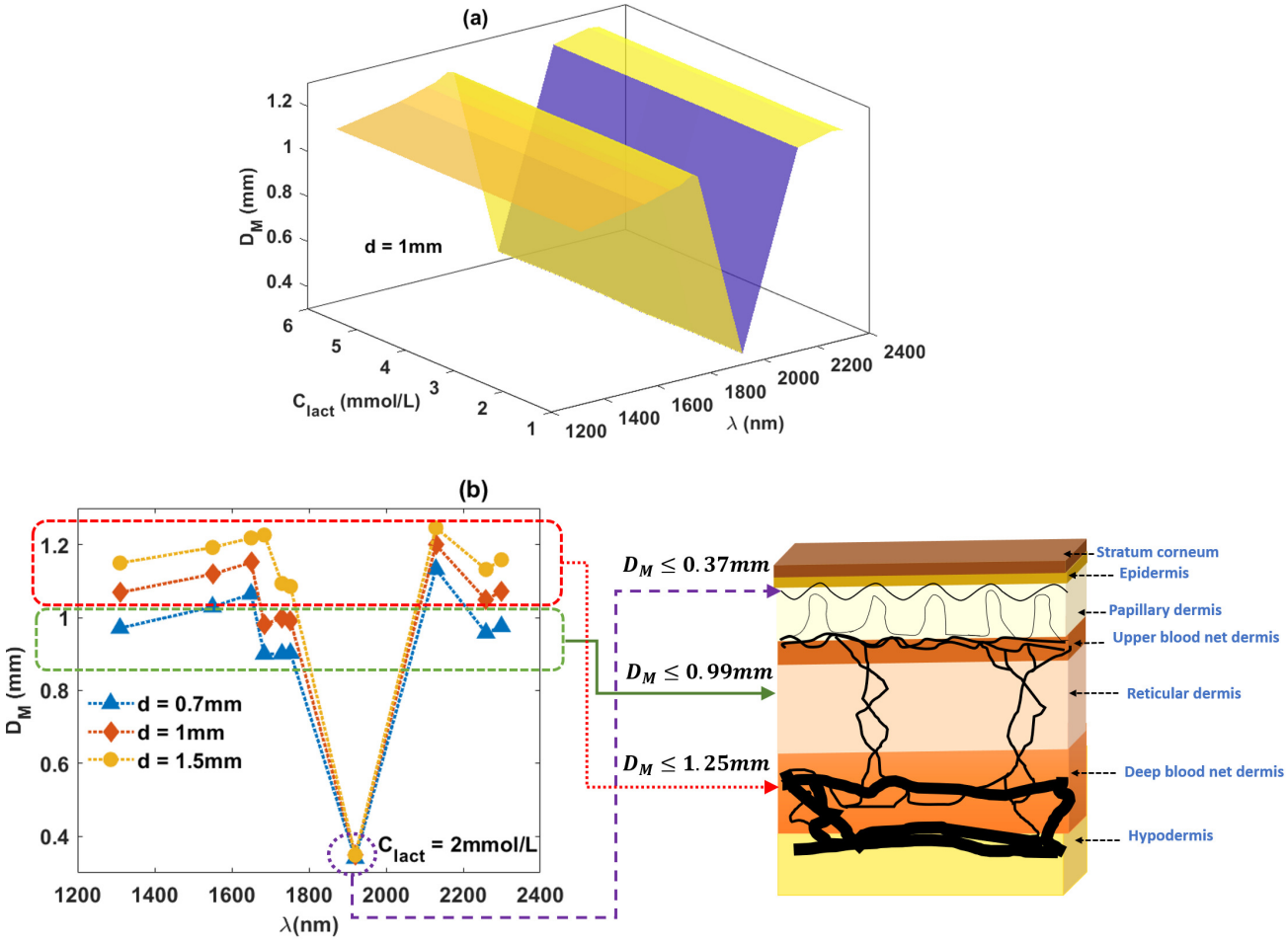


**Figure 4.** Monte Carlo simulated mean penetration depth ($D_M$) at SWIR. Simulated results at a fixed source-detector separation ($d = 1$ mm) for the varying lactate concentrations ($C_{lact} = 1, 2, 3, 4, 5, \& 6$ mmol/L) are shown in (a). Simulated results for the tissue with a nominal concentration of blood lactate ($C_{lact} = 2$ mmol/L) at three source-detector separations ($d =$ 0.7 mm, 1 mm, 1.5 mm) are presented in (b). The tissue volume interrogated at different sensor specifications are illustrated simultaneously. The magenta, green and red dotted lines correspond to three different combinations of characterizing wavelengths and source-detector separations.

The mean penetration depth ($D_M$), calculated as the mean of the maximum z-coordinate recorded through the path of each detected photon, gives an idea of the sample volume interrogated by the sensor. As shown in Figure 4, the penetration depth varies with wavelength and remains unchanged with the varying lactate concentration. Even though the penetration depth at SWIR does not increase as significantly as seen in the near-infrared region, still a gradual increment is found with the increasing source-detector separation. At 1920 nm, where the water absorbance is the highest, the depth of penetration is the lowest ($D_M \leq 0.37$ mm; within papillary dermis). With a source-detector separation of 0.7 mm and at wavelengths 1310 nm, 1550 nm, 1684 nm, 1730 nm, and 1752 nm, photons travel through the moderately vascularized reticular dermis ($D_M \leq 0.99$ mm). With the rest of the combinations of the sensor specifications, light penetrates through the deep blood net dermis ($D_M \leq 1.23$ mm) which contains the densest vascular network.

Simulated absorbance variation with wavelength and lactate concentration is presented in Figure 5(a). The simulated absorbance spectra resembling the water and lactate absorbance distribution is shown in Figure 1. With variations in lactate

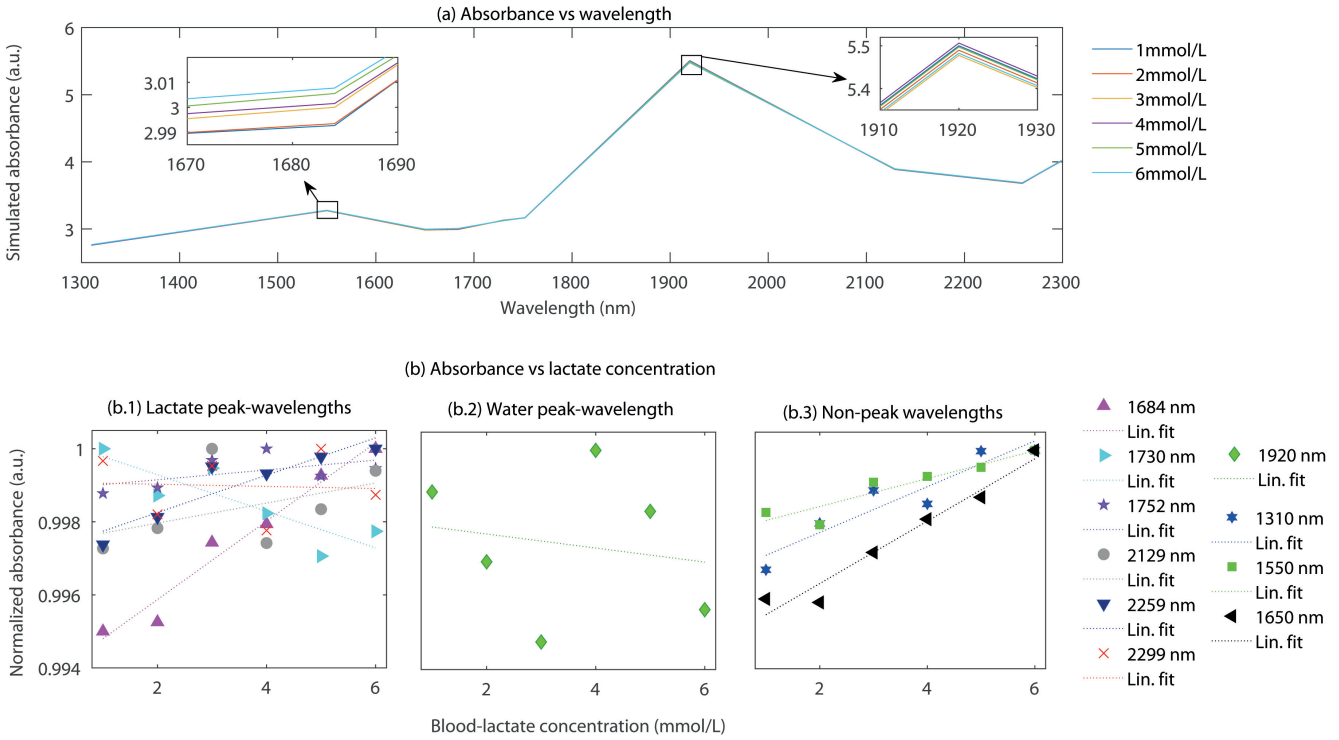


**Figure 5.** Absorbance spectra at SWIR optical wavelengths and lactate concentration. Variation in absorbance with the wavelength at $\lambda$ = 1310 nm, 1550 nm, 1650 nm, 1684 nm, 1730 nm, 1752 nm, 1920 nm, 2259 nm and 2299 nm is demonstrated in (a), and the variation with the lactate concentration ($C_{lact}$ = 1-6 mmol/L ) are displayed as insets. For further illustration, the wavelength sets were divided into three categories, and the variations in the normalized absorbances with lactate concentration are shown in (b.1) lactate peak wavelengths, (b.2) water peak wavelength, and (b.3) non-peak wavelengths. Absorbance at lactate-peak wavelengths exhibit non-linearity among the wavelengths. The water peak-wavelength exhibits random results and the non-peak wavelengths exhibit linearity. Simulations were carried out at a source-detector separation of 1mm.

concentration, small but detectable changes in absorbance are found. Simulated absorbance was comparable to the results published by Maruo et. al[22] and agree with our previous in-vitro study[5].

Further processing of the data revealed different trends of the absorbance variation at different wavelengths. As shown in Figure 5(b), the wavelengths were categorized in three sections: (b.1) lactate-peak wavelengths (1684 nm, 1730 nm, 1752 nm, 2129 nm, 2259 nm, and 2299 nm), (b.2) water peak wavelength (1920 nm), and (b.3) non-peak wavelengths (1310 nm, 1550 nm, and 1650 nm). The categories were chosen based on the absorbance peaks shown in Figure 1(a). The wavelength 1684 nm is shown to be the most sensitive to the lactate concentration variation. At the rest of the lactate-peak wavelengths, absorbance varies slowly or decreases with the lactate concentration which attributes to the prevailing lipid concentrations at those wavelengths. At the water peak-wavelengths, absorbance is random and not sensitive to the lactate concentrations. At the non-peak wavelengths, though no prominent peaks of lactate or water exists, the overall absorbance of lactate is higher compared to other absorbers such as water and lipid, resulting in a linear increase in absorbance with lactate concentration.

The relative power was calculated as a product of the relative detected intensity and the effective cross-sectional area of the detector. As seen in Table 2, the maximum power measured at the output of the sensor is 2.51% of the incident power. Output power significantly decreases at higher source-detector separations, for example, at 1684nm, the relative output power at 0.7mm, 1mm and 1.5mm separations are 1.28%, 0.81% and 0.55%, respectively. The overall power consumption is higher at wavelengths beyond 1752nm, with the minimum at 1920nm.

## Discussion

A careful choice of the source-detector separation and the operating wavelength is of utmost importance to detect the small-scale absorbance changes due to lactate in presence of the very strong water absorbance at the SWIR wavelength range. The MC results presented in this paper have been utilized to optimize the source-detector separation and the wavelength of a non-invasive

**Table 2.** Relative output power at different sensor specifications.

| Relative detected power (%) | | | |
|---|---|---|---|
| $\lambda$ $(nm)$ | $d = 0.7mm$ | $d = 1mm$ | $d = 1.5mm$ |
| 1310 | 2.51 | 1.74 | 1.04 |
| 1550 | 0.9 | 0.53 | 0.26 |
| 1650 | 1.57 | 1.03 | 0.57 |
| 1684 | 1.28 | 0.81 | 0.55 |
| 1730 | 0.91 | 0.52 | 0.28 |
| 1752 | 0.89 | 0.52 | 0.28 |
| 1920 | 1.67E-02 | 3.17E-03 | 3.86E-04 |
| 2129 | 0.27 | 0.13 | 4.80E-02 |
| 2259 | 0.35 | 0.17 | 8.06E-02 |
| 2299 | 0.19 | 8.03E-02 | 0.0284 |

optical sensor of lactate based on the three criteria as follow:

- **Reduced noise:** input light signal penetrates sufficiently deep to reach the vascular regions of skin, confirming the signal is coming from the blood-lactate and not the bloodless sublayers of skin such as stratum corneum or epidermis, in which case it would result in noise;
- **High sensitivity:** it enables capturing small changes in lactate concentration in blood;
- **Low power consumption:** the relative output power is adequately detectable by the sensor, i.e., the loss of power is kept to a minimum.

The sensor design optimisation, therefore, is to be carried out based on the qualitative and quantitative analysis on the $10 \times 3$ combinations of the sensor specifications. For example, light penetrates through the densest vasculature (deep blood net dermis) at a source-detector separation of 1.5 mm and wavelength of 2129 nm, making it a justified choice according to the first aforementioned criteria. However, the further the light penetrates through tissue, the higher is the power consumption. Consecutively, the output detected power at this combination of sensor specifications is as low as 0.0048% which does not satisfy the third aforementioned criteria.

After a careful assessment on the datasets, we conclude that the combination of $\lambda = 1684$ nm, $d = 1$mm are the most feasible choice for the sensor design. At 1mm separation distance, light penetrates through the well-perfused reticular dermis region, therefore, a noise-free signal can be acquired. The wavelength 1684 nm is the most sensitive to the lactate concentration changes in blood. The output power at this combination of specifications is approximately 1% of the input power which can be achieved utilizing the standard fiber-optic spectrophotometer probes.

A real-time detection of blood-lactate concentration appears to be challenging because of the high water absorbance and low signal strength. Recent advancements of silicon photonic chips and integrated spectrophotometers can be helpful in designing a robust lactate sensing technology. Also, the mixed trends found at different SWIR wavelengths with the lactate concentration variation indicate a non-linear relationship between the variables. Thus, the calibration of the sensor cannot be achieved through any standard regression analysis, and supervised machine learning algorithms must be incorporated. Observations from the in-silico investigations also agree with our previous experience where we explored a preliminary sophisticated algorithm to analyze our in-vitro experimental data[4].

## Conclusion

A robust three-dimensional heterogeneous Monte Carlo model of a tissue-ROI (i.e., human finger) was explored for the first time at the SWIR wavelengths to investigate the spectroscopic signature of blood-lactate. Simulated studies showed the details of light-tissue interactions at those wavelengths and optimized a source-detector separation of 1mm and a wavelength of 1684 nm as the best choice for detecting the lactate concentration changes. The information obtained from our in-silico investigation will be utilized for the future development of a novel integrated optical sensor for blood-lactate monitoring for the use in both clinical and homecare settings.

## References

1. Garcia-Alvarez, M., Marik, P. & Bellomo, R. Sepsis-associated hyperlactatemia. *Critical care* **18**, 1–11 (2014).

2. Baishya, N. *et al.* In-vitro spectrometric analysis of hyperlactatemia and lactic acidosis in buffer relating to sepsis. *J. Near Infrared Spectrosc.* 0967033520968951 (2020).
3. Baishya, N. *et al.* Comparison of dual beam dispersive and ftnir spectroscopy for lactate detection. *Sensors* **21**, DOI: 10.3390/s21051891 (2021).
4. Mamouei, M., Budidha, K., Baishya, N., Qassem, M. & Kyriacou, P. Comparison of wavelength selection methods for in-vitro estimation of lactate: a new unconstrained, genetic algorithm-based wavelength selection. *Sci. Reports* **10**, 1–12 (2020).
5. Budidha, K. *et al.* Identification and quantitative determination of lactate using optical spectroscopy—towards a noninvasive tool for early recognition of sepsis. *Sensors* **20**, 5402 (2020).
6. Baishya, N. *et al.* Investigations into the effects of ph on quantitative measurements of lactate in biological media using atr-ftir spectroscopy. *Molecules* **25**, 3695 (2020).
7. Lafrance, D., Lands, L. C., Hornby, L., Rohlicek, C. & Burns, D. H. Lactate measurement in whole blood using near infrared spectroscopy. *Can. J. Anal. Sci. Spectrosc.* **45**, 36–40 (2000).
8. Lafrance, D., Lands, L. C., Hornby, L. & Burns, D. H. Near-infrared spectroscopic measurement of lactate in human plasma. *Appl. Spectrosc.* **54**, 300–304 (2000).
9. Iida, T. *et al.* Monte carlo modeling of shortwave-infrared fluorescence photon migration in voxelized media for the detection of breast cancer. *Diagnostics* **10**, 961 (2020).
10. Iino, K. *et al.* Monte carlo simulation of near infrared reflectance spectroscopy in the wavelength range from 1000 nm to 1900 nm. *Opt. review* **10**, 600–606 (2003).
11. Zhang, H. *et al.* Penetration depth of photons in biological tissues from hyperspectral imaging in shortwave infrared in transmission and reflection geometries. *J. biomedical optics* **21**, 126006 (2016).
12. Wilson, R. H., Nadeau, K. P., Jaworski, F. B., Tromberg, B. J. & Durkin, A. J. Review of short-wave infrared spectroscopy and imaging methods for biological tissue characterization. *J. biomedical optics* **20**, 030901 (2015).
13. Wilson, R. H. *et al.* Quantitative short-wave infrared multispectral imaging of in vivo tissue optical properties. *J. biomedical optics* **19**, 086011 (2014).
14. Wang, R. K. & Tuchin, V. V. *Advanced biophotonics: tissue optical sectioning* (CRC Press, 2013).
15. Chatterjee, S., Budidha, K. & Kyriacou, P. A. Investigating the origin of photoplethysmography using a multiwavelength monte carlo model. *Physiol. Meas.* **41**, 084001 (2020).
16. Van Gemert, M., Jacques, S. L., Sterenborg, H. & Star, W. Skin optics. *IEEE Transactions on biomedical engineering* **36**, 1146–1154 (1989).
17. Simpson, C. R., Kohl, M., Essenpreis, M. & Cope, M. Near-infrared optical properties of ex vivo human skin and subcutaneous tissues measured using the monte carlo inversion technique. *Phys. Medicine & Biol.* **43**, 2465 (1998).
18. Jacques, S. L. Optical properties of biological tissues: a review. *Phys. Medicine & Biol.* **58**, R37 (2013).
19. Jacques, S. L. & McAuliffe, D. J. The melanosome: threshold temperature for explosive vaporization and internal absorption coefficient during pulsed laser irradiation. *Photochem. photobiology* **53**, 769–775 (1991).
20. Guillem, C., Zammit, P. & Harvey, A. R. Holistic monte-carlo optical modelling of biological imaging. *Sci. Reports (Nature Publ. Group)* **9** (2019).
21. Chen, A. I. *et al.* Multilayered tissue mimicking skin and vessel phantoms with tunable mechanical, optical, and acoustic properties. *Med. physics* **43**, 3117–3131 (2016).
22. Maruo, K. *et al.* Noninvasive blood glucose assay using a newly developed near-infrared system. *IEEE J. selected topics quantum electronics* **9**, 322–330 (2003).


## Author contributions statement

S.C. has implemented the model, performed the data analysis and written the manuscript. K.B. has participated in developing the model and analyzing the data. M.Q. has assisted with her experimental insights and past experiences in the field, and helped data interpretation. P.K. has overseen the investigation and helped data interpretation. All authors have reviewed the manuscript.

## Competing interests

The authors declare no competing interests.

# Figures

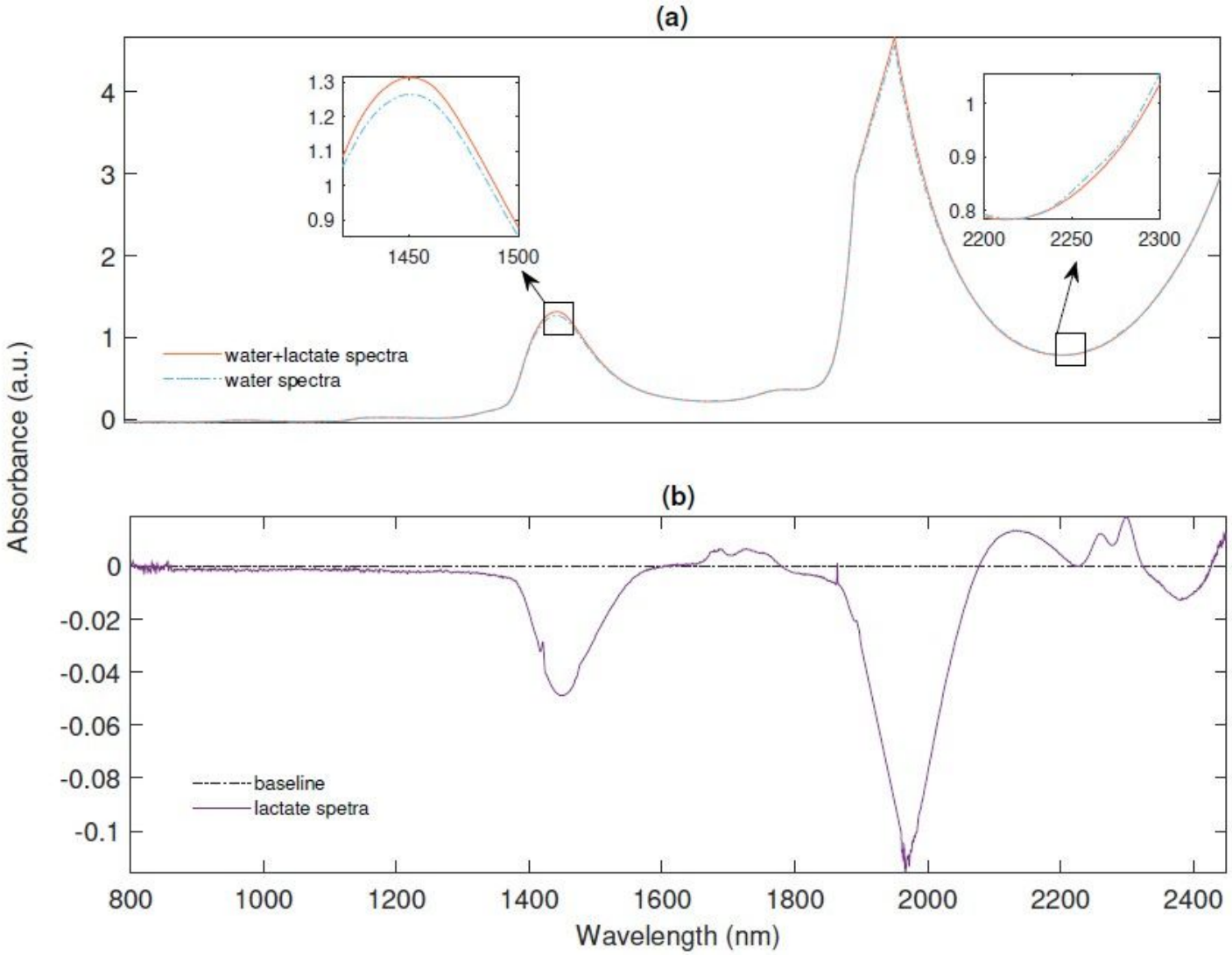


**Figure 1**

(a) The raw spectra of sodium L-lactate dissolved in aqueous PBS (concentration: 100 mmol/L) along with the spectra of just the aqueous PBS solution in the SWIR optical window. (b) Resultant spectra following the subtraction of aqueous PBS spectra from the lactate containing spectra.

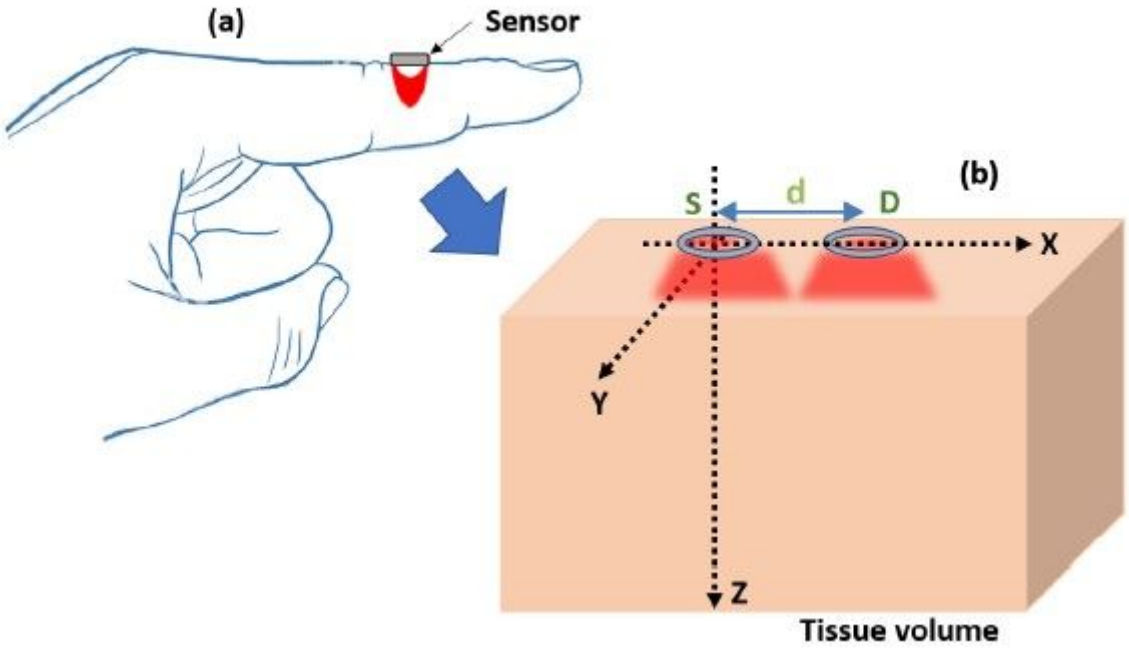


## Figure 2

Schematic of the sensor-tissue interaction platform. The ROI, i.e., a volume of human finger tissue interrogated by the sensor, is presented in the 3D Cartesian co-ordinate (XYZ) where the optical source (S) and detector (D) are respectively placed at the origin, and a distance d from it.

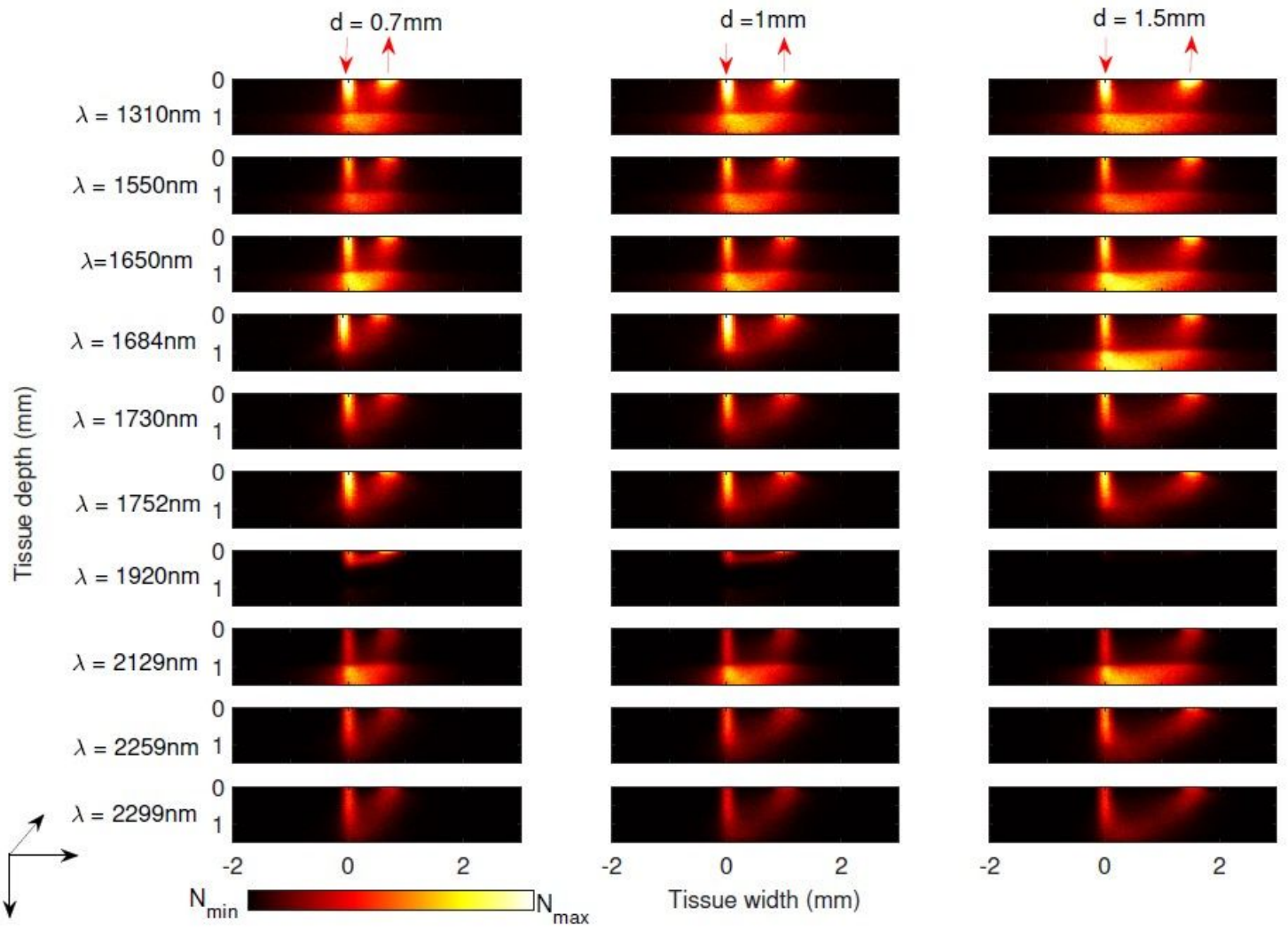


## Figure 3

Monte Carlo simulated light-tissue interaction profiles. The results show the distribution of the light-tissue interaction events in a reflectance mode optical sensor geometry having a source (downward red arrow) and a detector (upward red arrow). Results at three source-detector separations (d = 0:7mm; 1mm and 1:5mm) and the ten SWIR wavelengths (λ = 1310 nm, 1550 nm, 1650 nm, 1684 nm, 1730 nm, 1752 nm, 1920 nm, 2129 nm, 2259 nm and 2299 nm) are presented along the columns and the rows, respectively. The colorbar represents the number distribution of the interaction events (N) between its minimum and maximum values.

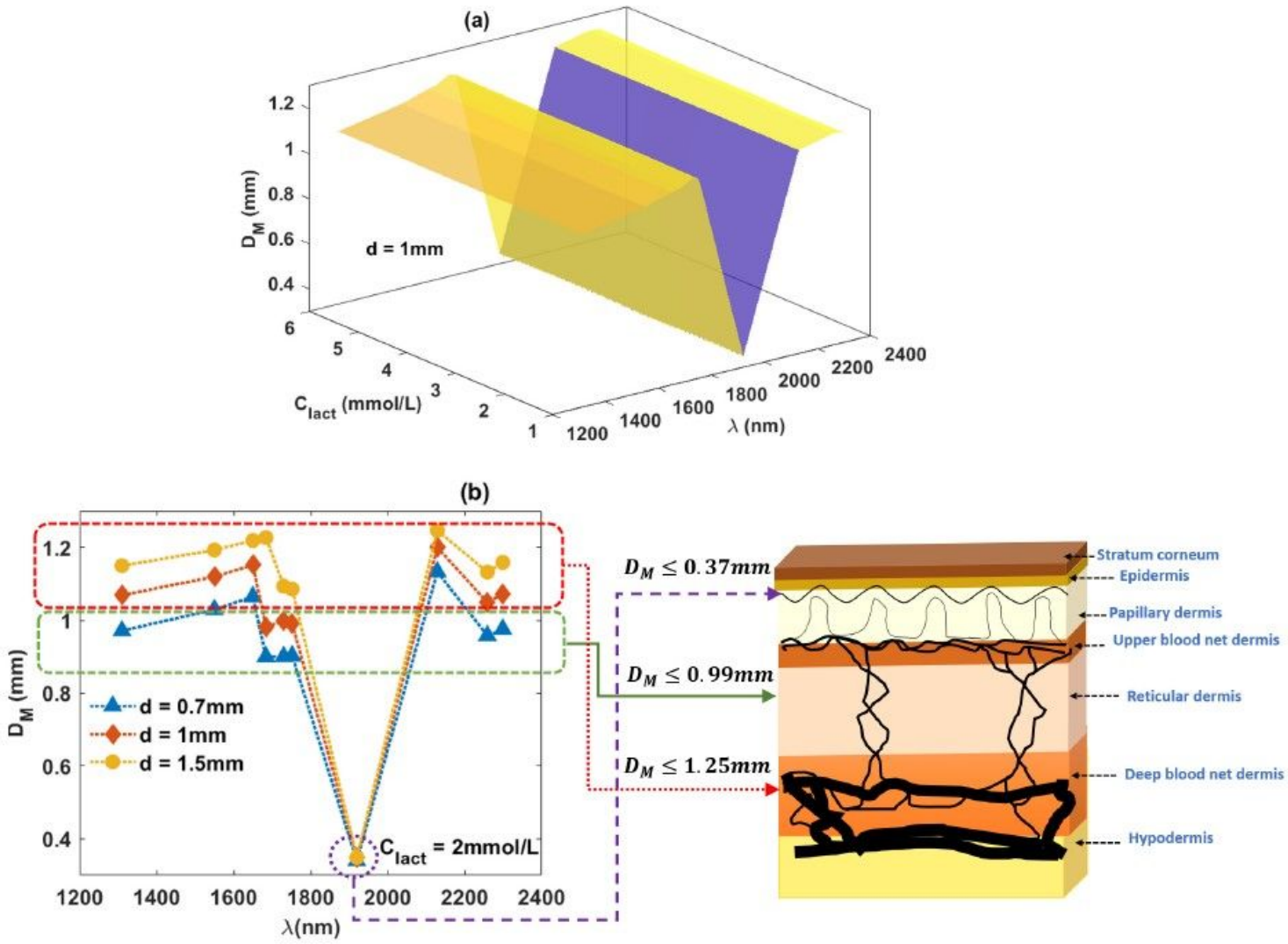


## Figure 4

Monte Carlo simulated mean penetration depth (DM) at SWIR. Simulated results at a fixed source-detector separation (d = 1 mm) for the varying lactate concentrations (Clact = 1, 2, 3, 4, 5, & 6 mmol/L) are shown in (a). Simulated results for the tissue with a nominal concentration of blood lactate (Clact = 2 mmol/L) at three source-detector separations (d = 0.7 mm, 1 mm, 1.5 mm) are presented in (b). The tissue volume interrogated at different sensor specifications are illustrated simultaneously. The magenta, green and red dotted lines correspond to three different combinations of characterizing wavelengths and source-detector separations.

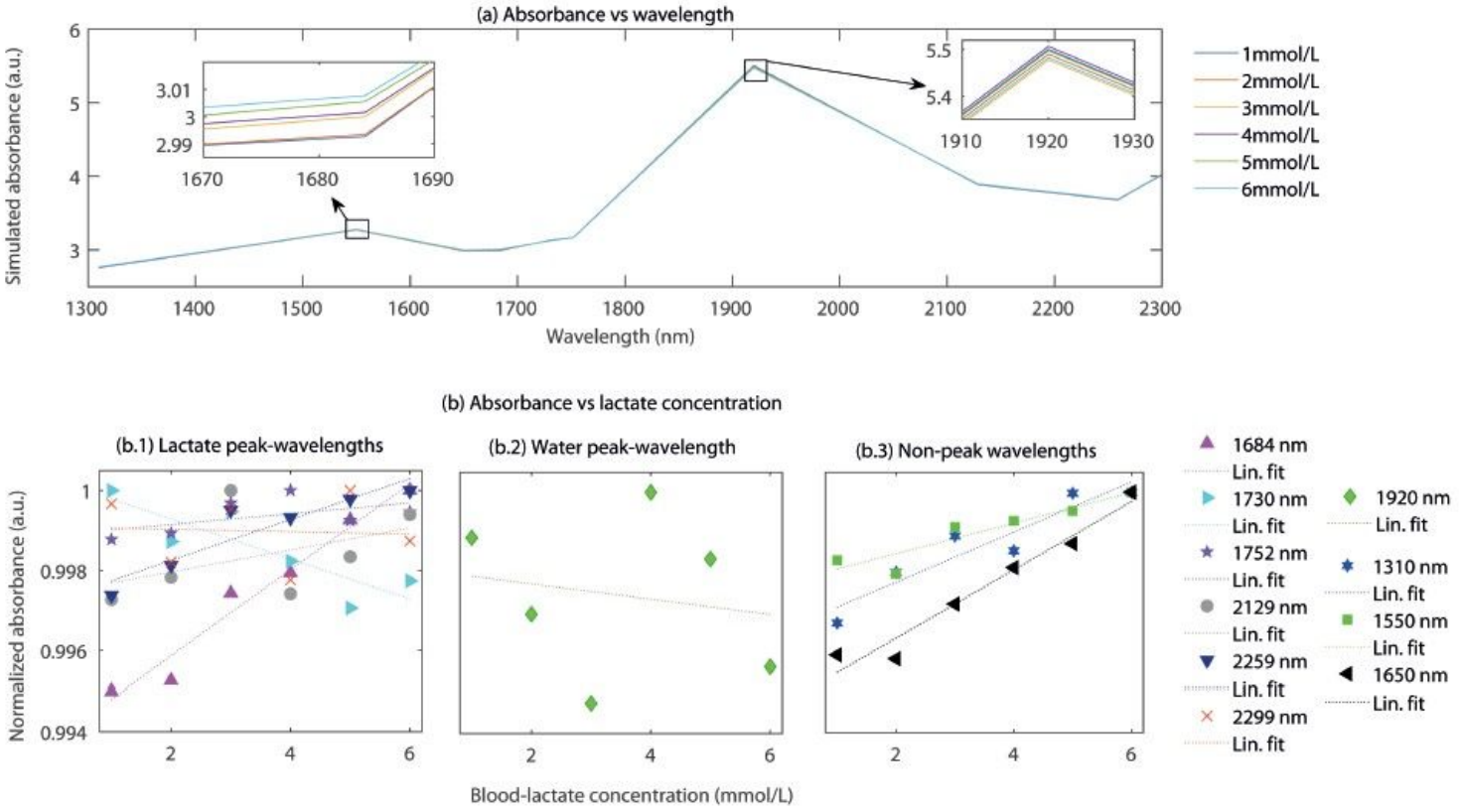


## Figure 5

Absorbance spectra at SWIR optical wavelengths and lactate concentration. Variation in absorbance with the wavelength at λ = 1310 nm, 1550 nm, 1650 nm, 1684 nm, 1730 nm, 1752 nm, 1920 nm, 2259 nm and 2299 nm is demonstrated in (a), and the variation with the lactate concentration (Clact = 1-6 mmol/L ) are displayed as insets. For further illustration, the wavelength sets were divided into three categories, and the variations in the normalized absorbances with lactate concentration are shown in (b.1) lactate peak wavelengths, (b.2) water peak wavelength, and (b.3) non-peak wavelengths. Absorbance at lactate-peak wavelengths exhibit non-linearity among the wavelengths. The water peak-wavelength exhibits random results and the non-peak wavelengths exhibit linearity. Simulations were carried out at a source-detector separation of 1mm.